EES Catalysis

COMMUNICATION

View Article Online
View Journal | View Issue

Check for updates

Cite this: *EES Catal.*, 2025, 3, 80

Received 6th July 2024,
Accepted 27th September 2024

DOI: 10.1039/d4ey00141a

rsc.li/eescatalysis

Interplanar synergy of a copper-based electrocatalyst favors the reduction of CO_2 into C_{2+} products†

Jiangnan Li,‡[a] Xinyi Duan,‡[c] Chao Wu,[ab] Yucheng Cao,[a] Zhiyao Duan,[c] Wenjun Fan,*[a] Peng Zhang*[b] and Fuxiang Zhang*[a]

Although electrocatalytic reduction of carbon dioxide (CO_2) into chemicals and fuels over Cu-based catalysts has been extensively investigated, the influence of their exposed facets on product selectivity remains elusive. To address this, a series of Cu-based catalysts with different ratios of exposed Cu(100) and Cu(111) facets were synthesized and examined for CO_2 electroreduction, based on which a remarkable interplanar synergistic effect on the selectivity of C_{2+} products was demonstrated. The optimized Cu-based interplanar synergistic catalyst could deliver a faradaic efficiency of 78% with a C_{2+} partial current density of 663 mA cm^{-2}, which is extremely superior to that of its corresponding Cu counterparts with only the Cu(111) or Cu(100) facet. The interplanar synergistic effect was disclosed using density functional theory calculations to mainly benefit from favorable adsorption and activation of CO_2 into *CO on the Cu(111) facet and significantly promoted C–C coupling on the interface of the Cu(111) and Cu(100) facets, as confirmed by observation of the favorable surface coverage of atop-bound and bridge-bound *CO as well as formation of *OC–CHO intermediates during *in situ* infrared spectroscopy analysis.

Broader context

Interplanar synergy of a copper-based electrocatalyst favors reduction of CO_2 into C_{2+} products carbon dioxide (CO_2) emissions pose significant environmental challenges, driving research into electrocatalytic methods for converting CO_2 into valuable chemicals and fuels. This approach not only addresses CO_2 emissions but also offers a sustainable pathway for energy conversion. Despite progress in generating carbon monoxide and formate from CO_2, achieving high selectivity for higher-value chemicals (C_{2+} products) remains a challenge due to complex reaction pathways and sluggish kinetics. Cu-based catalysts are pivotal in CO_2 electroreduction research. By synthesizing Cu-based catalysts with varying proportions of the exposed Cu(100) and Cu(111) facets, we identified a significant interplanar synergistic effect. This effect enhances the selectivity towards C_{2+} products, demonstrating promising advancements in sustainable chemical and fuel production. Our optimized Cu interplanar synergistic catalysts exhibited high faradaic efficiencies and current densities, surpassing those of catalysts dominated solely by the Cu(111) or Cu(100) facet. Theoretical calculations and experimental analysis corroborate these findings, highlighting the role of facet engineering in advancing CO_2 conversion technologies.

CO_2 conversion into value-added chemicals, powered by renewable electrical energy, offers a promising pathway for the generation of fuels and chemicals while concurrently mitigating CO_2 emissions.[1–3] To date, significant progress has been made in the electrochemical CO_2 reduction reaction (CO_2RR) to afford C_1 chemicals, particularly carbon monoxide and formate.[4–8] However, the generation of higher valued and energy-concentrated multicarbon (C_{2+}) molecules is still retarded by multi-electron transfer and sluggish C–C coupling kinetics.[9,10] Cu-based electrocatalysts are well-recognized for

---

[a] *State Key Laboratory of Catalysis, iChEM, Dalian Institute of Chemical Physics, Chinese Academy of Sciences, Dalian 116023, Liaoning, China. E-mail: wjfan@dicp.ac.cn, fxzhang@dicp.ac.cn*

[b] *School of Materials Science and Engineering, Zhengzhou University, Zhengzhou, 450001, China. E-mail: Zhangp@zzu.edu.cn*

[c] *State Key Laboratory of Solidification Processing, School of Materials Science and Engineering, Northwestern Polytechnical University, 710072 Xi'an, P. R. China. E-mail: zhiyao.duan@nwpu.edu.cn*

† Electronic supplementary information (ESI) available: The authors have cited additional references. See DOI: https://doi.org/10.1039/d4ey00141a

‡ These authors contributed equally to this work.

favoring the electrocatalysis of CO_2 to C_{2+} products,[11] and numerous strategies, including alloying,[12,13] surface modification,[14] and oxidation state tuning,[15,16] have been explored for the promoted selectivity of C_{2+} products. However, the selectivity of C_{2+} products is still not satisfactory owing to the challenging *CO surface coverage and/or sluggish C–C coupling.

The integration of Cu with a second electroactive component through rational tuning of the catalyst assembly has emerged as a highly effective strategy to trigger the production of multicarbon products. To date, synergistic catalysts for the CO_2RR with varied active compositions, including Cu^0/Cu^+,[17] Cu/metals (such as Ag, Au, and Zn),[18–20] Cu/molecules,[21] and Cu/carbon-based materials,[22–25] have been documented to effectively promote C_{2+} generation. Recently, the facets of Cu-based catalysts with distinct atom arrangements and surface energies have been demonstrated to remarkably affect the activity and selectivity of the CO_2RR.[26–28] For example, the Cu(111) facet was demonstrated to favor CO_2 protonation for selective production of CH_4, whereas the Cu(100) or Cu(110) facet is favorable for C–C coupling and the formation of C_2H_4 or oxygenates.[29–31] We speculated that the coexistence of these facets might leverage their complementary properties. This drove us to investigate whether a synergistic effect between the Cu(111) and Cu(100) or Cu(110) facet could enhance CO_2RR performance, particularly in terms of increasing the selectivity for C_{2+} products and improving the overall reaction yield. Herein, we experimentally confirmed the feasibility of the interplanar synergistic effect in improving the selectivity of the C_{2+} product during the alkaline CO_2RR processes of Cu-based catalysts with different ratios of Cu(111) and Cu(100) facets. Based on our optimization of the relative ratio of the exposed facets, the optimal Cu interplanar synergistic catalysts (CISCs) could deliver a C_{2+} FE of 83% in the H-type cell at a low overpotential, and the FE of C_{2+} products reached 78% with C_{2+} partial current density of 663 mA cm^{-2} in a flow cell. The synergistic effect was confirmed by both density functional theory calculations and experimental *in situ* surface-enhanced infrared absorption spectroscopy analysis.

As depicted in Fig. 1a, the CISCs were originated from the *in situ* electrochemical reduction of the Cu-based precursors, which were initially prepared using a facile precipitation method (supplementary Experimental section). For comparison, varied precipitation durations of 18, 24, 32, and 40 h were employed to synthesize the precursors, denoted as Cu-P18, Cu-P24, Cu-P32, and Cu-P40, respectively. Following the electrochemical treatment, the corresponding CISCs, separately denoted as CISC-18, CISC-24, CISC-32, and CISC-40, were prepared to obtain varying ratios of Cu(111) and Cu(100) facets. Based on our preferential performance optimization, the CISC-24 catalyst with optimal selectivity of the C_{2+} product was chosen as a typical synergistic catalyst for discussion. Meanwhile, the catalysts with exclusively Cu(111) or Cu(100) exposed facets were prepared[32] as the control samples (denoted as Cu(111)–C and Cu(100)–C, respectively), whose structures and morphologies were confirmed by X-ray diffraction (XRD) patterns and microscopic images (Fig. S1 and S2, ESI†),

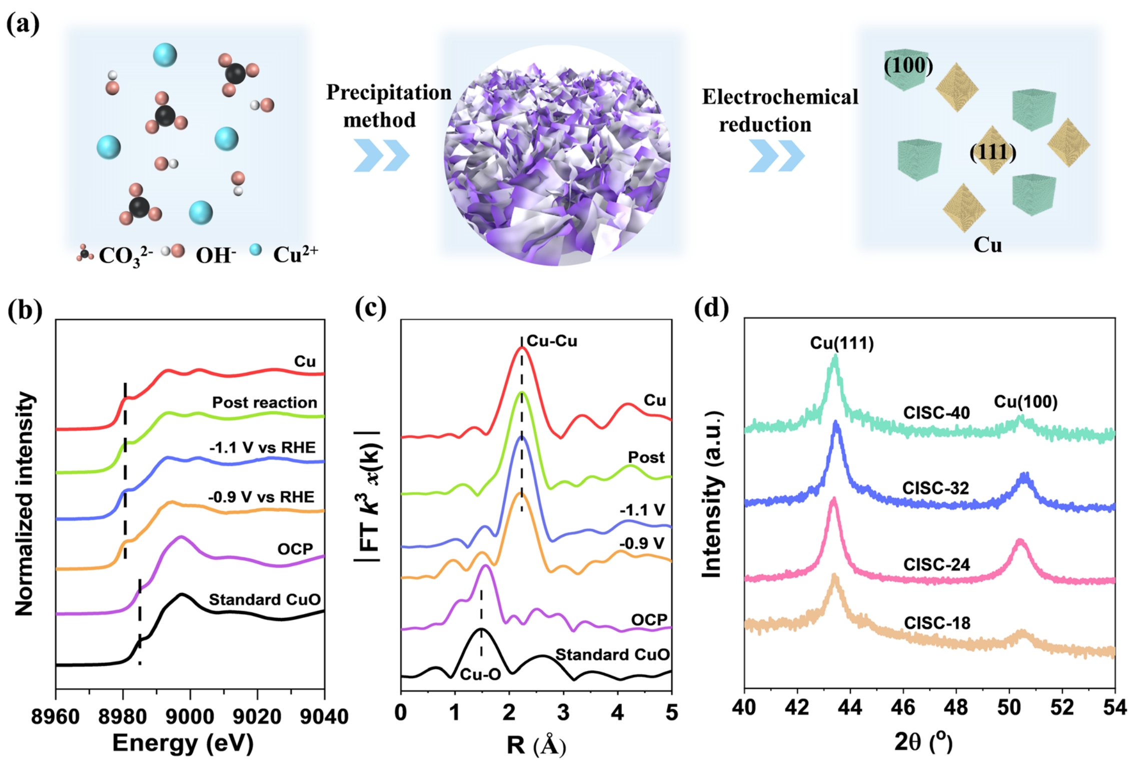

Fig. 1 (a) Schematics of the preparation of CISCs. *In situ* XAS measurement of CISC-24 on a carbon paper electrode under applied bias: (b) Cu K-edge XANES spectra and (c) Fourier-transform Cu K-edge EXAFS spectra. (d) XRD patterns of CISC-18, CISC-24, CISC-32 and CISC-40.

respectively. As shown in the scanning electron microscopy (SEM) images (Fig. S3, ESI†), the Cu-P24 precursor displays a nanosheet morphology, and its high-resolution TEM (HRTEM) image reveals its defective-rich structure with numerous pores of the nanosheets (Fig. S4, ESI†). The crystal phases of the precursor can be indexed as CuO according to its XRD patterns (Fig. S5, ESI†).

In situ X-ray absorption (XAS) spectroscopy analysis was carried out to gain an insight into the local structural evolution of the Cu-P24 precursor during the electrochemical reconstruction. As observed in the normalized Cu K-edge X-ray absorption near-edge spectra (XANES) (Fig. 1b), the structure and chemical state of the Cu-P24 precursor (OCP curve in Fig. 1b) undergo dynamic reconstruction upon electroreduction treatment at the applied potentials. Together with the scattering signal in the extended X-ray absorption fine structure (EXAFS) curves (Fig. 1c), it was confirmed that the CuO precursor was completely converted to metallic Cu(0) upon the applied bias. The structural evolution induced by the electrochemical reduction is supported by the change in the morphology (Fig. S6, ESI†). The formation of metallic copper can be further confirmed by the typical XRD patterns (Fig. 1d) and HRTEM images (Fig. 2). Based on the intensities of peaks in Fig. 1d, we estimated the relative ratios of Cu(100) to Cu(111) facets on CISCs, which exhibit an initial increase followed by a decrease as a function of the precipitation reaction time. This trend aligns with the results of HRTEM images, where the CISC-24 displays a significantly higher content of the Cu(100) facets (Fig. 2a) with respect to the CISC-40 sample (Fig. 2b).

The CO_2RR performance of CISC-24 was initially evaluated by linear sweep voltammetry (LSV) curves in an H-type cell reactor with CO_2-saturated 0.1 M $KHCO_3$ as the electrolyte. As given in Fig. S7 (ESI†), CISC-24 exhibits a notably superior current density to other CISCs or control catalysts (Cu(100)–C, Cu(111)–C). Moreover, all the CISCs display higher faradaic efficiency (FE) for C_{2+} products compared to the Cu(100)–C or Cu(111)–C samples with a single exposed facet (Fig. 3a and Fig. S8, ESI†), indicating the synergistic effect between the two facets.

Specifically, CISC-24 can deliver a C_{2+} FE of 83% with a C_{2+}/C_1 product ratio of *ca.* 17 at −1.1 V (Fig. 3a and b), extremely superior to that of the Cu(100)–C and Cu(111)–C catalysts with C_{2+}/C_1 product ratio of *ca.* 5 and 1, respectively. The synergistically promoted C_{2+} production is also reflected by the volcano-type dependence of FEs for C_{2+} products and the C_{2+}/C_1 ratio on a series of CISCs samples with varied Cu(100) to Cu(111) ratios (Fig. 3b).

To address the sluggish diffusion of CO_2 in the H-type cell, we thus evaluated the CO_2RR performance in a flow cell with 3 M KOH solution as the electrolyte. Typically, CISC-24 exhibits a sharp increase in the LSV current density under the flow of CO_2 compared with that in Ar flow (Fig. S9, ESI†), indicating its efficient CO_2 electroreduction. Strikingly, CISC-24 could deliver a C_{2+} FE of over 70% in a broad potential window from −0.49 to −0.72 V under high current densities ranging from 600 to 950 mA cm^{-2} (Fig. 3c). Specifically, the FE of C_{2+} products from CO_2RR of the CISC-24 catalyst reached 78.1% at −0.61 V with a partial current density of 663 mA cm^{-2}, which outperforms most of the reported Cu-based catalysts for C_{2+} generation (Table S1, ESI†). It is worth highlighting that CISC-24 is robust under the flow cell condition at a current density of 300 mA cm^{-2} (Fig. 3d), where the selectivity can be held at ∼75% without obvious change during the experimental time course. It should be pointed out that the decrease in the CO_2RR performance over prolonged periods primarily originates from the flooding of the electrolyte solution onto the gas diffusion layer (Fig. S10, ESI†) instead of the instability of the catalyst itself, as has been similarly observed in other flow-cell CO_2RR systems.[33] We have also conducted extended stability test in membrane electrode assembly (MEA) and observed that the catalyst maintains high stability for 20 hours (Fig. S11, ESI†).

To get insights into the synergistic promotion effect of Cu(111) and Cu(100) on the C_{2+} selectivity, *in situ* surface-enhanced

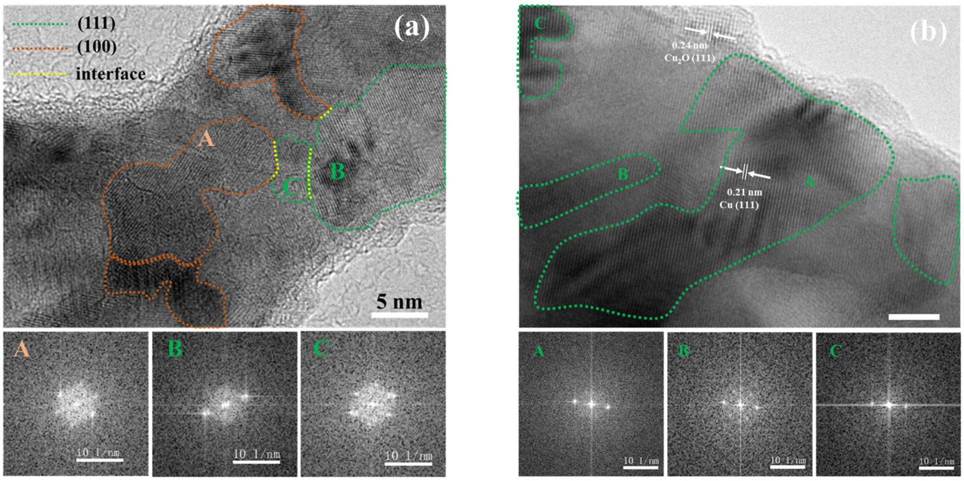

Fig. 2 Structural characterization of CISCs. (a) The HRTEM image of CISC-24. (b) The HRTEM image of CISC-40. Green and orange dotted lines circle areas of the Cu(111) and Cu(100) facets, respectively; yellow lines highlight the interfaces between the (111) and (100) facets. Below the HRTEM images, fast Fourier transforms (FFTs) of three typical areas are shown; orange letters represent Cu(100) and green letters represent Cu(111).

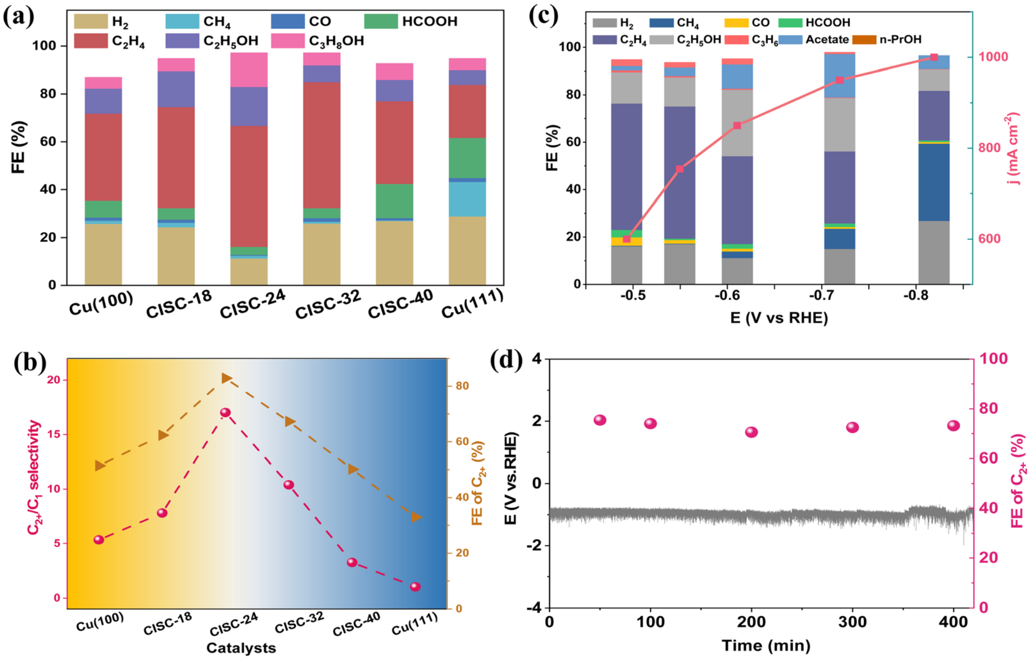

Fig. 3 CO_2RR performance. (a) Faradaic efficiency of various products at −1.1 V in the H-type cell; (b) faradaic efficiency of C_{2+} and product ratio of C_{2+}/C_1 on different types of Cu catalysts at −1.1 V; (c) faradaic efficiency of CISC-24 at various potentials in a flow cell. (d) Long-term CO_2RR stability test of Cu-24 in 1 M $KHCO_3$ electrolyte at a constant current density of 300 mA cm^{-2}.

infrared absorption spectroscopy with attenuated total reflection (ATR-SEIRAS) configuration was used to monitor the electrochemical intermediate formed on the surface of the catalysts (Fig. S12, ESI†). Besides the observation of a broadband at ∼1650 cm^{-1} attributed to the H–O vibration mode of adsorbed water on the surface of CISC-24 (Fig. 4a), additional bands located at 2040 cm^{-1}, 1806 cm^{-1}, 1761 cm^{-1}, 1550 cm^{-1} and 1370 cm^{-1} can be observed and assigned to the atop-bonded *CO (*CO_{atop}), bridge-bonded *CO (*CO_{bridge}), *CHO, *OCCHO and *COOH, respectively.[15,34] Comparatively, however, only *CO_{atop} is conspicuously observed on the Cu(100)–C and Cu(111)–C control samples (Fig. 4b and c).[35] It should be noted that the *CO and *CHO intermediates are key for the formation of *COCHO with C–C coupling as well as multi-carbon products;[36–38] thus, the shortage of the *CHO intermediate on the control samples results in their inferior C_{2+} selectivity. In addition, the *CO_{bridge} appears in the potential range from −0.76 V to −1.15 V and rapidly declines as the potentials are negatively moved, in accordance with the trend of FE for C_{2+} products on CISC-24. This reveals that the coexistence of *CO_{atop} and *CO_{bridge} is crucial for effective C–C coupling.[39] The observed coexistence of *CO_{atop} and *CO_{bridge} on CISC-24 also reassures the concurrent Cu(100)/Cu(111) facets in the catalyst since CO tends to be bound to the bridge and top sites on the Cu(100) and Cu(111) surfaces, respectively. Additionally, as displayed in Fig. 4d, the intensity of *CO coverage is gradually decreased as a function of time during the time-dependent ATR-SEIRAS measurement of CISC-24 at −1.15 V, while the *CO coverages on the control samples are slightly changed (Fig. S13 and S14, ESI†). On the basis of the above observation, it is reasonable to conclude that CISC-24 with coexisting Cu(100) and Cu(111) surfaces is more favorable for the activation of CO_2 and the C–C coupling with respect to the single planar Cu(100)–C or Cu(111)–C sample, which should be responsible for its remarkably promoted selectivity toward C_{2+} products.

To elucidate the underlying mechanism for enhancing the production of the C_{2+} species on the CISC-24 catalyst, density functional theory (DFT) calculations were conducted. The employed models of Cu(111) and (100) with the adsorbed intermediates are illustrated in Fig. 5a and more detailed atomic structures are given in Tables S2 and S3 (ESI†). As seen in Fig. 5b, the free energies for the formation of *COOH on the Cu(111) and Cu(100) facets are almost identical, whereas the free energy for *CO formation on the Cu(111) surface is approximately 0.2 eV lower than that on the Cu(100) surface. Moreover, the exothermic free energy change at U = 0 V demonstrates favorable CO_2 conversion into *CO on both Cu(111) and Cu(100) facets. However, the generation of dissolved CO species, *i.e.*, CO desorption, is very difficult on both the facets because of the strong adsorption of *CO with a binding energy of CO below −1.0 eV.

To investigate the interplanar synergistic effects between the Cu(111) and Cu(100) surfaces, an atomistic model of the Cu(111)/(100) interfacial system was constructed (Fig. S15, ESI†). Various binding sites in the vicinity of the Cu(111)/(100) interface for CO adsorption were examined, and the calculated CO adsorption energies, plotted as a function of distance from the interfacial line in the specified direction, are presented in Fig. 5c. Evidently, CO exhibits stronger binding at the interface with respect to the Cu(111) and (100) facets. Consequently, it is posited that the interface functions as a

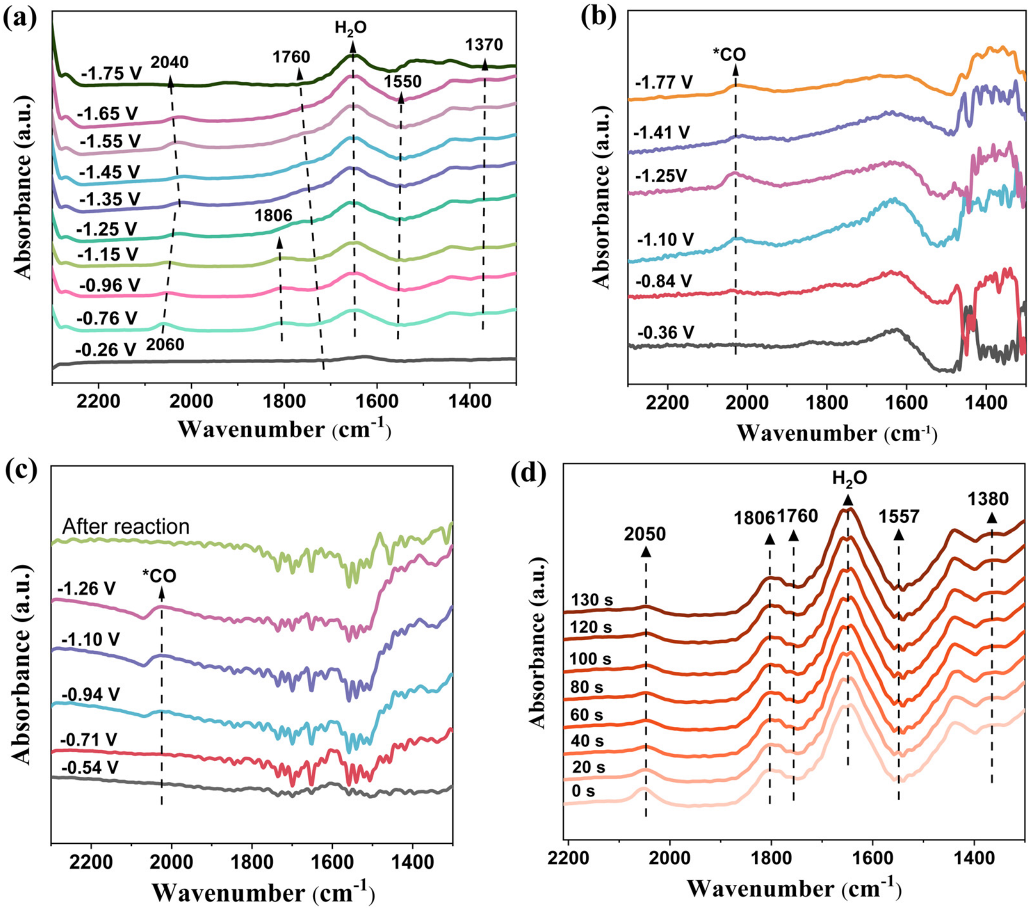

Fig. 4 *In situ* ATR-SEIRAS studies for the detection of reaction intermediates of the CO_2RR over typical samples at different polarization potentials: (a) CISC-24; (b) Cu(100)–C; (c) Cu(111)–C. (d) Time-dependent ATR-SEIRAS spectra obtained on the CISC-24 sample at −1.15 V.

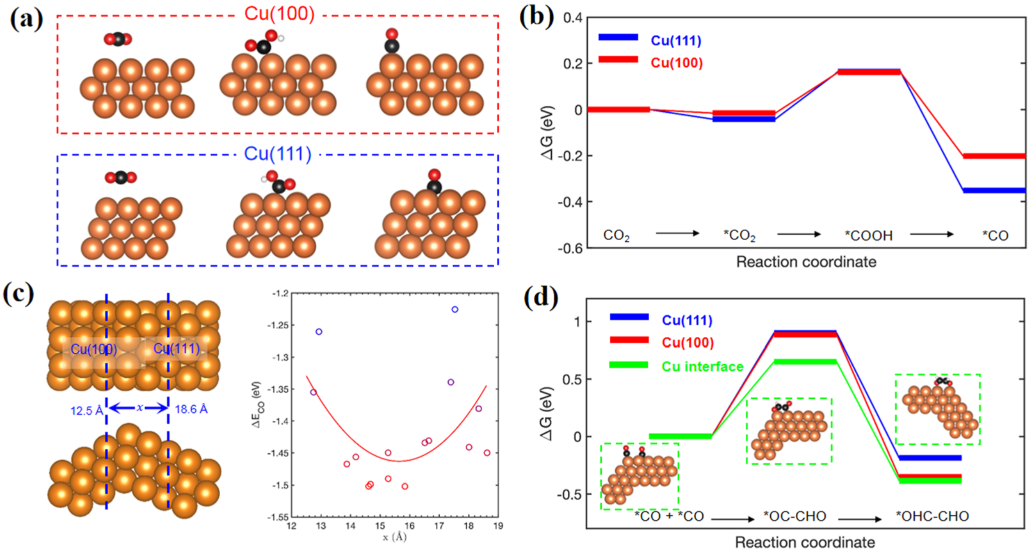

Fig. 5 DFT calculations. (a) DFT models of Cu with different facets. (b) Free energy diagram for CO_2 reduction into *CO on the Cu(111) and (100) surfaces at U = 0 V. (c) CO adsorption energy in the vicinity of the Cu(111)/(100) interface. (d) Free energy diagram for reductive CO–CO coupling on Cu(111), Cu(100) and Cu(111)/(100) interface at U = 0 V.

thermodynamic sink for *CO generated on the facets. To validate this hypothesis, free energy diagrams for the reductive CO–CO coupling process were constructed on Cu(111), Cu(100), and the Cu(100)/(111) interface, as depicted in Fig. 5d. The detailed atomic structures of the adsorbed intermediates are provided in Tables S2–S6 (ESI†). During this process, two adjacent *CO molecules are cooperatively coupled and converted into *OC–CHO, consistent with the results of ATR-SERIES (Fig. 4). As shown in Fig. 5d, the free energy change for *OC–CHO formation on the Cu(100)/(111) interface is much lower compared to that on the Cu(111) or Cu(100) facets. Overall, DFT calculations substantiate that the Cu(111)/(100) interface exhibits a pronounced affinity for *CO, leading to the promoted concentration of *CO, the pivotal intermediate *OC–CHO as well as promoted the C–C coupling process for the formation of C_{2+} products.

In summary, we have demonstrated the highly selective electrocatalytic reduction of CO_2 into multicarbon products by the interplanar synergistic effect of Cu(100) and Cu(111) facets, which could effectively promote the C–C coupling as well as selectivity of CO_2RR into C_{2+} products, delivering a faradaic efficiency of 78% and partial current density of 663 mA cm^{-2} at −0.61 V *vs.* RHE. As confirmed by ATR-SERIES characterization and DFT calculation, the synergy between Cu(100) and Cu(111) is demonstrated to increase the surface *CO coverage of $*CO_{atop}$ and $*CO_{bridge}$, further promoting the formation of the adsorbed intermediate *COCHO and facilitating the C–C coupling kinetics, which should be responsible for the remarkably promoted selectivity of C_{2+} products. Our results provide an alternative way of developing efficient electrocatalysts toward long-chain chemicals by the synergy of interplanar synergistic catalysis.

Data availability

All data supporting the findings of this study are included in the main text and its ESI.† Additionally, the original experimental data can be accessed from the corresponding author to ensure transparency and support further research endeavors. Please contact Zhang Fuxiang at fxzhang@dicp.ac.cn.

Conflicts of interest

The authors declare no conflict of interest.

Acknowledgements

This work was supported by the National Key R&D Program of China (2020YFA0406102), the Strategic Priority Research Program of the Chinese Academy of Sciences (No. XDB 0600100), and the National Natural Science Foundation of China (22261160369, 22005301). Z. D. acknowledges the support from the National Natural Science Foundation of China (Grant No. 52272238), the Natural Science Foundation of Shaanxi Province (Grant No. 2022JM-097). We gratefully acknowledge Shanghai Synchrotron Radiation Facility (beamline BL14W) for providing beam time.

References

1 M. Jouny, W. Luc and F. Jiao, *Ind. Eng. Chem. Res.*, 2018, **57**, 2165–2177.

2 S. Nitopi, E. Bertheussen, S. B. Scott, X. Liu, A. K. Engstfeld, S. Horch, B. Seger, I. E. L. Stephens, K. Chan, C. Hahn, J. K. Nørskov, T. F. Jaramillo and I. Chorkendorff, *Chem. Rev.*, 2019, **119**, 7610–7672.

3 J. L. White, M. F. Baruch, J. E. Pander, Y. Hu, I. C. Fortmeyer, J. E. Park, T. Zhang, K. Liao, J. Gu, Y. Yan, T. W. Shaw, E. Abelev and A. B. Bocarsly, *Chem. Rev.*, 2015, **115**, 12888–12935.

4 S. Ren, D. Joulié, D. Salvatore, K. Torbensen, M. Wang, M. Robert and C. P. Berlinguette, *Science*, 2019, **365**, 367–369.

5 M. Liu, Y. Pang, B. Zhang, P. De Luna, O. Voznyy, J. Xu, X. Zheng, C. T. Dinh, F. Fan, C. Cao, F. P. G. de Arquer, T. S. Safaei, A. Mepham, A. Klinkova, E. Kumacheva, T. Filleter, D. Sinton, S. O. Kelley and E. H. Sargent, *Nature*, 2016, **537**, 382–386.

6 N. Han, Y. Wang, H. Yang, J. Deng, J. Wu, Y. Li and Y. Li, *Nat. Commun.*, 2018, **9**, 1320.

7 L. Li, A. Ozden, S. Guo, F. P. García de Arquer, C. Wang, M. Zhang, J. Zhang, H. Jiang, W. Wang, H. Dong, D. Sinton, E. H. Sargent and M. Zhong, *Nat. Commun.*, 2021, **12**, 5223.

8 T. Zheng, C. Liu, C. Guo, M. Zhang, X. Li, Q. Jiang, W. Xue, H. Li, A. Li, C.-W. Pao, J. Xiao, C. Xia and J. Zeng, *Nat. Nanotechnol.*, 2021, **16**, 1386–1393.

9 D. Gao, R. M. Arán-Ais, H. S. Jeon and B. Roldan Cuenya, *Nat. Catal.*, 2019, **2**, 198–210.

10 A. D. Handoko, F. Wei, Jenndy, B. S. Yeo and Z. W. Seh, *Nat. Catal.*, 2018, **1**, 922–934.

11 A. A. Peterson, F. Abild-Pedersen, F. Studt, J. Rossmeisl and J. K. Nørskov, *Energy Environ. Sci.*, 2010, **3**, 1311–1315.

12 T. T. H. Hoang, S. Verma, S. Ma, T. T. Fister, J. Timoshenko, A. I. Frenkel, P. J. A. Kenis and A. A. Gewirth, *J. Am. Chem. Soc.*, 2018, **140**, 5791–5797.

13 Y. C. Li, Z. Wang, T. Yuan, D.-H. Nam, M. Luo, J. Wicks, B. Chen, J. Li, F. Li, F. P. G. de Arquer, Y. Wang, C.-T. Dinh, O. Voznyy, D. Sinton and E. H. Sargent, *J. Am. Chem. Soc.*, 2019, **141**, 8584–8591.

14 A. K. Buckley, M. Lee, T. Cheng, R. V. Kazantsev, D. M. Larson, W. A. Goddard Iii, F. D. Toste and F. M. Toma, *J. Am. Chem. Soc.*, 2019, **141**, 7355–7364.

15 T.-C. Chou, C.-C. Chang, H.-L. Yu, W.-Y. Yu, C.-L. Dong, J.-J. Velasco-Vélez, C.-H. Chuang, L.-C. Chen, J.-F. Lee, J.-M. Chen and H.-L. Wu, *J. Am. Chem. Soc.*, 2020, **142**, 2857–2867.

16 P.-P. Yang, X.-L. Zhang, F.-Y. Gao, Y.-R. Zheng, Z.-Z. Niu, X. Yu, R. Liu, Z.-Z. Wu, S. Qin, L.-P. Chi, Y. Duan, T. Ma, X.-S. Zheng, J.-F. Zhu, H.-J. Wang, M.-R. Gao and S.-H. Yu, *J. Am. Chem. Soc.*, 2020, **142**, 6400–6408.

17 G.-Y. Duan, X.-Q. Li, G.-R. Ding, L.-J. Han, B.-H. Xu and S.-J. Zhang, *Angew. Chem., Int. Ed.*, 2022, **61**, e202110657.

18 C. Chen, Y. Li, S. Yu, S. Louisia, J. Jin, M. Li, M. B. Ross and P. Yang, *Joule*, 2020, **4**, 1688–1699.

19 D. Ren, B. S.-H. Ang and B. S. Yeo, *ACS Catal.*, 2016, **6**, 8239–8247.

20 C. G. Morales-Guio, E. R. Cave, S. A. Nitopi, J. T. Feaster, L. Wang, K. P. Kuhl, A. Jackson, N. C. Johnson, D. N. Abram, T. Hatsukade, C. Hahn and T. F. Jaramillo, *Nat. Catal.*, 2018, **1**, 764–771.

21 F. Li, Y. C. Li, Z. Wang, J. Li, D.-H. Nam, Y. Lum, M. Luo, X. Wang, A. Ozden, S.-F. Hung, B. Chen, Y. Wang, J. Wicks, Y. Xu, Y. Li, C. M. Gabardo, C.-T. Dinh, Y. Wang, T.-T. Zhuang, D. Sinton and E. H. Sargent, *Nat. Catal.*, 2020, **3**, 75–82.

22 X. Wang, J. F. de Araújo, W. Ju, A. Bagger, H. Schmies, S. Kühl, J. Rossmeisl and P. Strasser, *Nat. Nanotechnol.*, 2019, **14**, 1063–1070.

23 D. Chen, L.-H. Zhang, J. Du, H. Wang, J. Guo, J. Zhan, F. Li and F. Yu, *Angew. Chem., Int. Ed.*, 2021, **60**, 24022–24027.

24 D.-L. Meng, M.-D. Zhang, D.-H. Si, M.-J. Mao, Y. Hou, Y.-B. Huang and R. Cao, *Angew. Chem., Int. Ed.*, 2021, **60**, 25485–25492.

25 H. Wang, Y.-K. Tzeng, Y. Ji, Y. Li, J. Li, X. Zheng, A. Yang, Y. Liu, Y. Gong, L. Cai, Y. Li, X. Zhang, W. Chen, B. Liu, H. Lu, N. A. Melosh, Z.-X. Shen, K. Chan, T. Tan, S. Chu and Y. Cui, *Nat. Nanotechnol.*, 2020, **15**, 131–137.

26 A. Loiudice, P. Lobaccaro, E. A. Kamali, T. Thao, B. H. Huang, J. W. Ager and R. Buonsanti, *Angew. Chem., Int. Ed.*, 2016, **55**, 5789–5792.

27 Z. W. Ulissi, M. T. Tang, J. Xiao, X. Liu, D. A. Torelli, M. Karamad, K. Cummins, C. Hahn, N. S. Lewis, T. F. Jaramillo, K. Chan and J. K. Nørskov, *ACS Catal.*, 2017, **7**, 6600–6608.

28 W. Luo, X. Nie, M. J. Janik and A. Asthagiri, *ACS Catal.*, 2016, **6**, 219–229.

29 Y. Huang, A. D. Handoko, P. Hirunsit and B. S. Yeo, *ACS Catal.*, 2017, **7**, 1749–1756.

30 Y. Hori, A. Murata and R. Takahashi, *J. Chem. Soc., Faraday Trans.*, 1989, **85**, 2309–2326.

31 Y. Hori, I. Takahashi, O. Koga and N. Hoshi, *J. Phys. Chem. B*, 2002, **106**, 15–17.

32 W. Luc, X. Fu, J. Shi, J.-J. Lv, M. Jouny, B. H. Ko, Y. Xu, Q. Tu, X. Hu, J. Wu, Q. Yue, Y. Liu, F. Jiao and Y. Kang, *Nat. Catal.*, 2019, **2**, 423–430.

33 W. Lai, Y. Qiao, Y. Wang and H. Huang, *Adv. Mater.*, 2023, **35**, 2306288.

34 S. Zhu, T. Li, W.-B. Cai and M. Shao, *ACS Energy Lett.*, 2019, **4**, 682–689.

35 W. Luc, X. Fu and J. Shi, *et al.*, Two-dimensional copper nanosheets for electrochemical reduction of carbon monoxide to acetate, *Nat. Catal.*, 2019, **2**, 423–430.

36 K. J. P. Schouten, Z. Qin, E. Pérez Gallent and M. T. M. Koper, *J. Am. Chem. Soc.*, 2012, **134**, 9864–9867.

37 J. D. Goodpaster, A. T. Bell and M. Head-Gordon, *J. Phys. Chem. Lett.*, 2016, **7**, 1471–1477.

38 F. Pan, X. Duan, L. Fang, H. Li, Z. Xu, Y. Wang, T. Wang, T. Li, Z. Duan and K.-J. Chen, *Adv. Energy. Mater.*, 2024, **14**, 2303118.

39 H. Zhang and Y.-M. Yan, *ACS Appl. Energy Mater.*, 2023, **6**, 11448–11457.